Chapter 2
Critical Issues in Oxide-Semiconductor Heteroepitaxy

In semiconductor/semiconductor heteroepitaxy, assuming that one is able to grow the correct phase of the material using the appropriate growth conditions, the two main challenges are the lattice and thermal mismatches between the substrate and the growing film [1]. Extensive work has been dedicated to address these difficulties including the lattice grading method [2], and the use of a compliant substrate for strain management [3]. The latter approach is based on a free, single crystal membrane that is sufficiently thin to deform elastically, thus allowing for total strain to be shared between the membrane and the heteroepitaxial layer grown upon it. These concepts have been utilized to reduce the defects in a variety of materials systems such as SiGe/SOI/Si [4], InGaAs/GaAs [5], and GaN/SOI [6] (SOI stands for silicon on insulator).

Thermal mismatch is an even a bigger problem in oxide-semiconductor integration because the difference in thermal expansion coefficients is greater. For example, the thermal expansion of Si is $2.6 \times 10^{-6}\ K^{-1}$ and it is $8.8 \times 10^{-6}\ K^{-1}$ in $SrTiO_3$ (STO). In other words at the growth temperature a semiconductor is slightly larger than what it is at room temperature, while the oxide is significantly larger, and thus one would expect large stresses to develop in the film upon cooling. As we shall see later in the book, this thermal mismatch has a real effect on the properties of thin oxide films grown on semiconductors at high temperature. On the one hand, one might exploit this difference. On the other hand, this makes low temperature deposition methods, such as atomic layer deposition (ALD) very attractive.

Luckily, nature gives us a break and lattice mismatch is a much less critical problem when depositing oxide films compared to semiconductor films. As semiconductors are mostly simple sp^3 covalently bonded materials, they are very sensitive to interatomic angles, and have a limited range of structural responses to lattice mismatch. Covalently bonded materials can only strain so much before they will relax to their normal lattice spacing, most commonly by forming edge dislocations that glide to the substrate-film interface. This concept is captured in the famous Matthews-Blakeslee model that relates the critical thickness of an epitaxial film to elastic strain, assuming that strain is relieved only through dislocation

A.A. Demkov and A.B. Posadas, *Integration of Functional Oxides with Semiconductors*, DOI 10.1007/978-1-4614-9320-4_2, © The Author(s) 2014

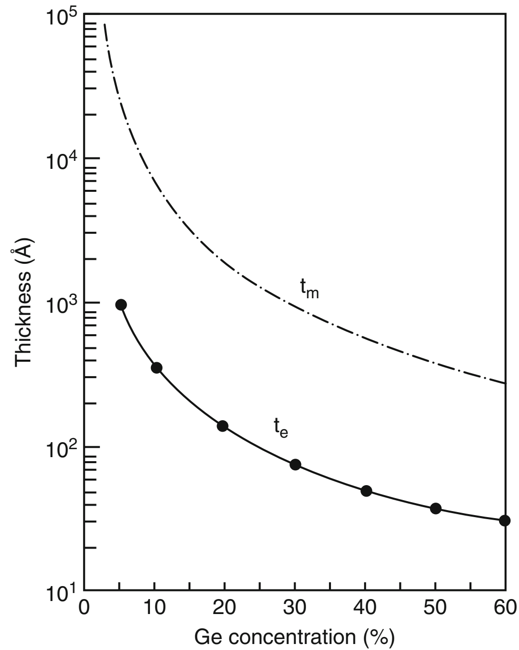

Fig. 2.1 Matthews-Blakeslee model for $Si_{1-x}Ge_x$ on Si. The *lower curve* is the equilibrium critical thickness from the model while the *upper curve* is a metastable condition calculated for growth at 500 °C. Copyright IOP Publishing. Reproduced from [9] by permission of IOP Publishing. All rights reserved

formation [7, 8]. The Matthews-Blakeslee equation (simplified for pure edge misfit dislocations) states that the critical thickness h_c can be expressed as:

$$h_c = \frac{b}{4\pi f(1+\nu)}\left[ln\left(\frac{h_c}{b}\right)+1\right]$$

Here f is the lattice mismatch; ν is the Poisson's ratio, and b is the Burgers vector of the misfit dislocation. The resulting curve for SiGe/Si is shown in Fig. 2.1 [9]. One can see that a strain of ~1 % (Ge content of 25 %) results in a critical thickness of ~10 nm and a strain of ~2 % (Ge content of 50 %) results in a critical thickness of ~4 nm.

Oxides are generally more tolerant of strain than semiconductors. Perovskite oxides being partly ionic are somewhat less sensitive to bond angle variation as long as the interatomic distances are maintained (Coulomb interaction depends mainly on the absolute distance between the charges). Also, perovskites have a much broader arsenal of responses at their disposal. Some are due to their more complicated crystal structure, and some to the peculiarity of transition metals. First, as we have discussed in Chap. 1, the octahedra can rotate and tilt which gives the oxide some freedom to change volume. Second, for certain transition metal ions, the octahedra can change its "stiffness" by changing the spin state of the transition metal ion, allowing the octahedra to distort. Third, lattice parameters of an oxide can often change by introducing oxygen vacancies into the crystal structure [10]. In other words, there are internal degrees of freedom that allow the material to lower

its energy in response to strain [11]. As a result, it is not uncommon to epitaxially grow pseudomorphic oxide films with as much as several percent lattice mismatch to relatively large thicknesses exceeding the predicted critical thickness [12–14].

There are, however, three additional key problems unique to heteroepitaxy of perovskite oxides with covalent semiconductors. For high quality films the layer-by-layer or Frank-Van der Merwe growth is necessary. This is controlled by wetting at the oxide/semiconductor interface and is intimately related to the chemical bonding at the interface. Despite the fact that it is possible to match an oxide lattice to that of a semiconductor in the plane, there still is a problem of growing over a step edge, as the surface step height of the substrate is not necessarily matched by the out-of-plane inter-planar distance of the film. Last but not least, there is a symmetry difference between, for example, the diamond lattice of Si and the simple cubic lattice of a perovskite. This symmetry mismatch may result in twin and other domains, which could adversely affect the film properties. In the case of Si, the additional problem is oxidation and etching. At low pressure, oxygen etches Si owing to volatility of SiO, leaving craters on the surface [15, 16], while at higher pressure the formation of an amorphous SiO_2 layer destroys any possibility of epitaxial registry.

Here we will focus on the fundamental issues of oxide/semiconductor epitaxy, using $SrTiO_3$ on Si and GaAs as examples. However, these problems are universal and apply to all other systems discussed in this book, with the caveat that symmetry mismatch does indeed depend on the actual symmetry of the crystal and the types of domains possible on hexagonal substrates are different from those on a diamond or zincblende substrate.

2.1 Lattice Matching Oxides and Semiconductors

Looking at the diamond crystal structure of Si and ABO_3 perovskite structure of STO in Chap. 1, one is intrigued how exactly these two can be matched. The answer is given in Fig. 2.2. Si atoms at the surface are depicted with large spheres and smaller spheres correspond to atoms below the surface, with depth marked in units of lattice constant *a*. As can be seen from the figure, the surface unit cell of unreconstructed Si(001) is rotated 45° with respect to the conventional cubic cell of Si owing to the face-centered cubic (fcc) nature of the Si lattice. The lattice constant of a 1×1 surface cell is $a/\sqrt{2}$ or 3.84 Å, which is very close to 3.905 Å of cubic STO and results in 1.66 % compressive strain in a fully epitaxial oxide layer. This type of matching is often called a 45° rotation and is common to all perovskite on diamond (001) or zincblende (001) epitaxy. The critical thickness of STO on Si has been experimentally found to be approximately 4 nm [17].

Matching is of course different for the (111) orientation of cubic crystals [18, 19] or for hexagonal epitaxy [20]. For example, in Fig. 2.3 we illustrate the one-on-four lattice matching of cubic anti-bixbyite Gd_2O_3 on Si (111). Three stable phases of Gd_2O_3 can be found at ambient pressure. At room temperature, the cubic $Ia\overline{3}$ form is stable. It is followed by a monoclinic $C2/m$ phase at 1,500 K and hexagonal $P\overline{3}m1$

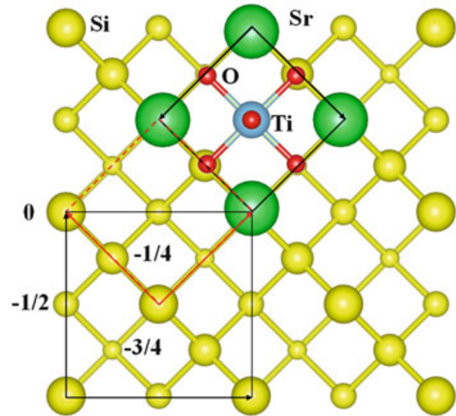

Fig. 2.2 Epitaxial matching of STO and Si (001). The 1 × 1 Si surface unit cell (*colored red*) is rotated 45° with respect to the bulk cubic cell (*colored black*) and matches the perovskite. The *numbers* refer to the vertical position with respect to the surface set at zero, in the units of Si lattice constant a = 5.43 Å

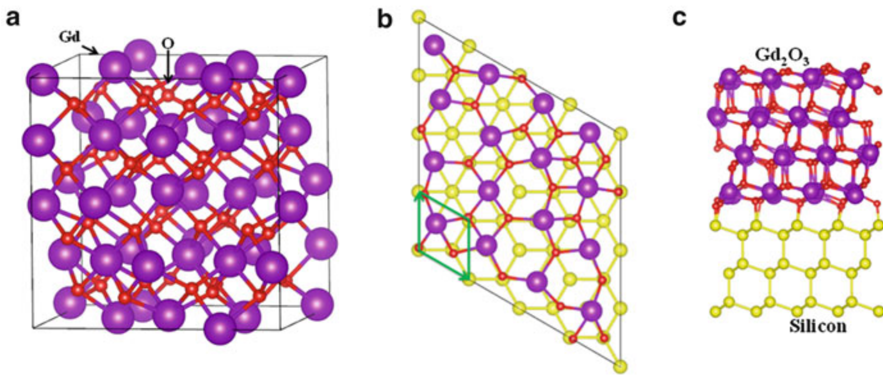

Fig. 2.3 Epitaxial matching of cubic Gd_2O_3 to Si (111). (**a**) Cubic unit cell of Gd_2O_3; (**b**) matching of one (111) unit cell of Gd_2O_3 to four unit cells of Si (111) (top view; Si unit cell is marked in *green*); (**c**) same matching, a side view along $(\bar{1}11)$

phase at 2,443 K. The ground state cubic phase of Gd_2O_3 is paramagnetic, but shows complex non-collinear antiferromagnetic behavior below 1.6 K [21, 22]. It is a large band gap (5.9 eV) insulator [23] with a medium dielectric constant $\varepsilon = 14$. The lattice constant of cubic Gd_2O_3 is 10.817 Å [24], and one unit cell of the (111) surface matches four unit cells of Si in the same orientation as shown in Fig. 2.3.

2.2 Wetting

The fundamental difficulty of perovskite/semiconductor epitaxy lies in thermodynamics. To achieve layer-by-layer growth, the film should wet the substrate. Wetting is controlled at the microscopic level by the interatomic forces. Knowing the surface energies of the substrate and film, and the energy of the interface

Table 2.1 Absolute surface energies $E_{surf}^{n\times m}$ and $\gamma^{n\times m}$ for various orientations and reconstructions

		E_{surf} (eV/1 × 1 cell)			γ (J/m^2)		
Orientation	Reconstruction	C	Si	Ge	C	Si	Ge
(111)	Unrelaxed	2.735	1.435	1.128	8.12	1.82	1.32
	Relaxed	2.165	1.372	1.116	6.43	1.74	1.30
	2 × 1 (right)	1.369	1.141	0.901	4.06	1.45	1.05
	2 × 1 (left)	1.369	1.136	0.893	4.06	1.44	1.04
	c(2 × 8)	2.346	1.109	0.865	6.96	1.41	1.01
	7 × 7	2.395	1.073	0.872	7.11	1.36	1.02
	H-covered	−2.760	−2.383	−2.249	−8.19	−3.03	−2.63
(110)	Unrelaxed	4.115	2.630	2.127	7.48	2.04	1.51
	Relaxed	3.264	2.190	1.661	5.93	1.70	1.17
	H-covered	−5.496	−4.644	−4.637	−9.99	−3.61	−3.32
(100)	Unrelaxed	3.780	2.174	1.691	9.72	2.39	1.71
	Relaxed	3.655	2.173	1.690	9.40	2.39	1.71
	2 × 1	2.222	1.321	1.035	5.71	1.45	1.05
	c(4 × 2)	2.222	1.285	0.985	5.71	1.41	1.00
	H-covered	−3.545	−4.853	−4.25	−9.11	−5.34	−4.56

Table taken from [25]

(γ_{sub}, γ_{film} and $\gamma_{\text{interface}}$, respectively), the condition of wetting can be simply expressed as:

$$\gamma_{sub} > \gamma_{film} + \gamma_{\text{inter}face} \tag{2.1}$$

In other words, to achieve wetting the substrate should have high surface energy γ_{sub}, the film should have low surface energy γ_{film}, and the cost of having an interface $\gamma_{\text{interface}}$ should be low. Interestingly, it follows from this inequality that if material A (the film) wets material B (the substrate), then B is unlikely to wet A. In semiconductor/semiconductor epitaxy, the surface energies of the film and the substrate are often reasonably close. In Table 2.1 we list surface energies of common semiconductors for low index surfaces from [25]. More importantly, the nature of chemical bonding is only slightly modulated across the interface, staying predominantly covalent. This results in an interface energy that is relatively small. Consequently, achieving wetting is relatively easy, provided the surface energy of the growing film can be kept low under the growth conditions (sometimes a surfactant is required), and the main concern is the lattice mismatch resulting in too much elastic energy being stored in the film. In contrast, for semiconductor/perovskite epitaxy, none of this is generally true. In particular, the energy cost of going from an ionic oxide to a covalent semiconductor is rather high. One, therefore, has to be creative in designing template or wetting layers to reduce the normally high interfacial energy.

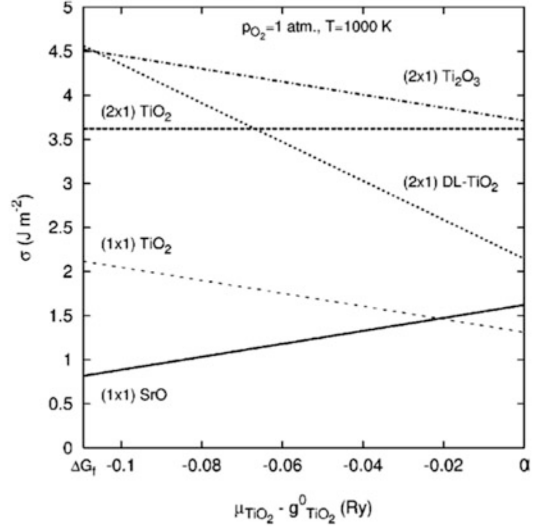

Fig. 2.4 Surface energies as a function of μ_{TiO_2} at T = 1,000 K and p_0 = 1 atm. Reprinted with permission from [28]. Copyright 2004 by the American Physical Society

Fortunately, the ABO_3 perovskite structure offers two (SrO and TiO_2) possible surface terminations and the surface energy is highly tunable [26–28]. Being a multicomponent system, the energy depends not only on the orientation and reconstruction, but also on the chemical environment as captured by the corresponding chemical potentials. In Fig. 2.4 we reproduce the surface energy diagram for STO from [28]. They considered 1 × 1 and 2 × 1 reconstructions of the (001) STO surface using first-principles DFT calculations. Surface energies were calculated as a function of TiO_2 chemical potential, oxygen partial pressure and temperature. The 1 × 1 unreconstructed surfaces were found to be energetically stable for many of the conditions considered. Under conditions of very low oxygen partial pressure, the 2 × 1 Ti_2O_3 reconstruction reported by Castell [29] was found stable. The graph corresponds to an oxygen pressure of 1 atm. and temperature of 1,000 K. Note the very wide range of surface energy from less than 1.0 to 4.5 J/m^2, and its sensitivity to the environment. The zero of chemical potential corresponds to TiO_2-rich environment.

Knowing surface energies, one can easily estimate what should be the energy of the interface to guarantee layer by layer growth. For example, for STO to wet Si, the surface energy of STO plus the energy of the interface should not exceed the surface energy of Si of ~1.7 J/m^2. With the STO surface energy ranging from 0.8 to almost 2.0 J/m^2 depending on the environment, this requires an interface with energy below 0.9 J/m^2 to achieve wetting [27]. This has been realized using a $SrSi_2$ template that has the stoichiometry of a bulk Zintl-Klemm intermetallic [30–33]. It is worth noting that this template also suppresses oxidation of Si below about 400 °C.

Recently, Demkov et al. explored theoretically the fundamental question of the bonding character change across the epitaxial interface between STO and GaAs

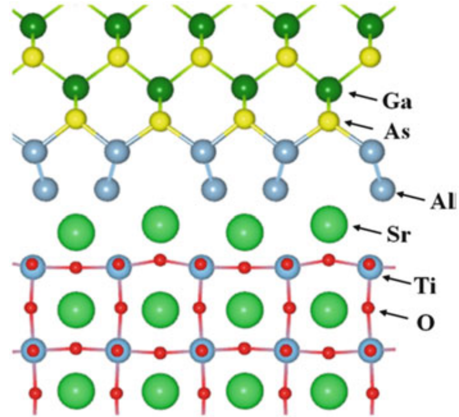

Fig. 2.5 Theoretical model of the STO/GaAs interface with a Zintl-Klemm $SrAl_2$ interlayer. Reprinted with permission from [34]. Copyright 2012, AIP Publishing LLC

using intermetallic Zintl-Klemm (Z-K) compounds as transition layers to ensure wetting [34]. The structure of cubic STO may be thought of as consisting of two types of alternating layers, a covalent TiO_2 layer and an ionic SrO layer. On the other hand, GaAs has zincblende structure, which is a manifestation of the sp^3 hybridization. Therefore, to form a high quality stable interface between a transition metal oxide material such as STO and an sp^3 covalent semiconductor such as GaAs, one has to change the fundamental nature of chemical bonding across the interface. If not addressed properly, this discontinuity in the chemical bonding results in a high interfacial energy γ_{int} of a few J/m^2. This high interfacial energy rather than the lattice mismatch is the main cause of 3D growth in perovskite/semiconductor epitaxy. Sr aluminides such as $SrAl_2$ offer a possible transition layer. Sr aluminide belongs to the Ae-Tr group of Zintl phases formed by triels and alkaline earths. The charge is transferred from the electropositive element Sr to the more electronegative element Al. Formally, Al^- has Si character, and forms structures characteristic to Si, i.e. diamond structure. For example, in the hypothetical cubic B32 (NaTl) structure Al atoms form a diamond-like four-connected network (see Chap. 1). In other words, the charge transfer from the electropositive to the electronegative species allows the latter one to assume the structural motif typical of Si, the next column element in the periodic table. It is precisely this property of Zintl compounds that can be exploited at the oxide/semiconductor interface.

In Fig. 2.5 we show the GaAs-STO interface proposed in [34]. The aluminide layer produced by replacing oxygen with Al in the SrO layer immediately following the TiO_2 surface plane serves as a transition from the d-orbital dominated bonding in the covalent octahedral Ti-O network to the tetrahedral network of AlAs. Note that AlAs is lattice matched to GaAs. The $SrAl_2$ interlayer separates STO from GaAs. GaAs is strained to match the STO lattice (a_{theory} = 3.87 Å). The Ga-As bond length in the bulk GaAs region ranges from 2.44 to 2.42 Å. At the interface the Al-As bond length is 2.42 Å, while the weaker Al-Al bonds in the Z-K layer are

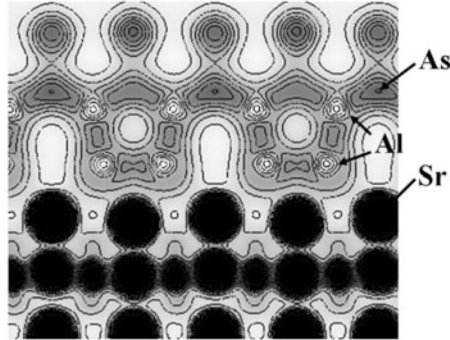

Fig. 2.6 Cross section of the charge distribution across the STO/Z-K/GaAs interface. The saturation level is set to 0.7 eÅ^{-3} (=12.6 % of the maximum density). The contours step interval is 0.05 eÅ^{-3}. Note the accumulation of charge between Al atoms representing the "covalent-like" Zintl-Klemm bonding. Reprinted with permission from [34]. Copyright 2012, AIP Publishing LLC

2.65 Å and 2.82 Å (to be compared to 2.82 Å in bulk $SrAl_2$). In Fig. 2.6, we show the charge density distribution in the plane containing Sr and Al atoms, with the contour plot overlaid. For clarity, the density saturation level is set to 0.7 eÅ^{-3} (12.6 % of the maximum charge density). Note the areas of relatively high electron density between the two Al atoms in the $SrAl_2$ interlayer. This pile up of charge is a Z-K bond between two metal atoms. The strength of these bonds is relatively low, as indicated by the low electron density.

Using the theoretical values for the surface energy of GaAs from [35], Demkov and co-workers assumed the average value of 1.0 J/m^2 representative of β2(2 × 4) reconstruction, which is stable in a wide range of As chemical potential. Then under Ti rich conditions the surface energy of STO is approximately 1.25 J/m^2 resulting in wetting of GaAs by STO as the mixed dimer (2 × 4) GaAs termination is stabilized. This is because under As and Ti rich conditions, the energy of the Zintl-based interface can be as low as 0.30 J/m^2. Indeed, Liang an co-workers have reported high quality epitaxial STO films on GaAs [36]. In addition, Demkov et al. computed the valence band offset at the GaAs/$SrTiO_3$ interface to be 2.50 eV in good agreement with recent experimental results [37]. Interestingly, the results of Demkov and co-workers also suggest a window for GaAs to wet STO which provides an explanation for the reported epitaxial growth of GaAs on STO, including a functional MESFET device [31].

Bulk properties of $SrAl_2$ were investigated theoretically by Slepko and Demkov [38]. They reported a density functional investigation of the orthorhombic (*Imma*) and cubic ($Fd\overline{3}m$) phases of this strontium aluminide. For the orthorhombic phase they calculated the work function and surface energy for (001), (010) and (100) oriented surfaces. The work function varies between 2.0 and 4.1 eV, and was shown to be determined by the predominant atomic species on the surface. Surface energy ranges from 0.32 to 1.84 J/m^2 were reported. More recently, Schlipf et al. have reported epitaxial growth by MBE of Zintl-phase $SrAl_4$ on the (001) oriented perovskite oxide $LaAlO_3$ using MBE [39]. Photoelectron spectroscopy measurements verified the Zintl-Klemm nature of the bonding in the material.

2.3 Kinetics Versus Thermodynamics: Chemical Reactivity

Even if the issues concerning lattice matching and wetting have somehow been resolved, the success of an epitaxial growth process is still dependent on an even more basic issue: thermodynamic stability of the film when in contact with the substrate at the growth conditions. For example, if the film reacts with the substrate while the film is growing and the reaction product is not lattice matched or does not wet the substrate then any chance for epitaxial growth is completely gone. This fundamental restriction severely limits the combinations of film and substrate materials that one can use to form epitaxial systems. Because many of the interesting functional oxides are ternary compounds, the relevant phase diagrams between them and semiconductors are often not yet completely mapped out adding to the difficulty of developing a process. It is for these reasons why there are very few epitaxial oxide on semiconductor systems that have been achieved to date. However, if we take advantage of the possibility of kinetic inhibition of some of these reactions between the substrate and the constituents of the oxide film, we may be able to work around some of these problems.

Let us look at the case of STO grown on Si by (see Chaps. 4 and 6 for details of the growth process). STO is an oxide where both metals are in their highest oxidation states. Depending on the arrival rates of the metals, there is a minimum oxygen partial pressure at which one is able to fully oxidize each metal. For a Ti metal flux of about one monolayer per minute, this pressure is experimentally found to be around $1–2 \times 10^{-6}$ Torr [40]. Once formed, TiO_2 itself is stable against reduction down to oxygen partial pressures of ~7×10^{-9} Torr at 750 °C and $<1 \times 10^{-15}$ Torr at 500 °C, based on the heat of formation of TiO_2. This fact strongly hints that it is kinetics (the arrival rate of atoms), not thermodynamics that determines whether a material forms during MBE growth. Comparatively, Sr is much easier to oxidize than Ti. Sr needs a mere ~1×10^{-8} Torr oxygen partial pressure to form SrO at a rate of about one monolayer per minute [41]. Once formed, SrO is very difficult to reduce back to Sr metal unless one goes to temperatures above 1,000 °C under ultrahigh vacuum conditions. Therefore, in order to grow STO by MBE at one monolayer per minute, we need an oxygen pressure of about 2×10^{-6} Torr. Another critical growth parameter is the substrate temperature. The substrate temperature must be such that there is high surface diffusion but the bulk diffusion remains negligible. These criteria define a temperature window for layer-by-layer growth. For ionically bonded materials like SrO, the window is fairly wide and spans from about 1/9 to 1/3 the melting point [42]. For SrO with a melting point of ~2,900 K, this means an optimum growth temperature of 320–970 K (50–700 °C). For covalently bonded materials like TiO_2, the window is narrower ranging from about half the melting point to just below the melting point [42]. With a melting point of 2,130 K, this means an optimum growth temperature for TiO_2 of at least 1,065 K (~790 °C). As the two windows do not overlap, we take the midpoint of the gap and say 740 °C is the optimum STO

growth temperature. Experimentally, however, because STO is not really $SrO + TiO_2$, the true growth window for layer-by-layer growth is more relaxed and flat STO can be grown at somewhat lower substrate temperature and oxygen partial pressure than in our simplified analysis [43], especially when co-depositing Sr and Ti where Ti oxidation is catalyzed by the presence of Sr, which is similar to the effect of using alkali metals to catalyze aluminum oxidation [44].

The growth conditions discussed above work very well when growing STO on STO substrates (homoepitaxy) but not necessarily on other substrates, particularly those that react readily with oxygen. We still have not yet addressed the issue of thermodynamic stability of the entire system during deposition. The bare Si substrate will rapidly form half a monolayer of amorphous SiO_2 when exposed for ~10 s to an oxygen pressure of 2×10^{-6} Torr at room temperature [45]. The substrate is not thermodynamically stable in the presence of oxygen but we need some minimum amount of oxygen to form the oxide film! This is the main problem that has prevented the development of epitaxially integrated oxides on silicon, and this is the problem to which the Zintl template provides a solution. While the detailed mechanism is still not clear at present, the half-monolayer Sr deposited on the Si(001) surface serves to protect the underlying Si from oxidation at modest temperatures and oxygen partial pressures. The Sr template has been found to be able to withstand conditions of up to ~400 °C and ~5×10^{-8} Torr O_2 for at least several minutes, keeping the oxygen on the surface and not allowing it to react with silicon [46]. The other key feature of the Sr Zintl template is that it preserves the surface lattice of silicon, allowing for epitaxy to occur.

We should note that even though the Sr Zintl template can withstand the presence of some oxygen at moderate temperatures, these conditions are still not optimal for layer-by-layer STO growth. The way around this is to kinetically limit Si oxidation in the presence of the template layer. We allow oxygen sufficient to oxidize a SrO layer but not to destroy the Zintl template into the growth chamber (~1×10^{-8} Torr) at a relatively low temperature (~200 °C). We then deposit Sr under this low oxygen partial pressure, which becomes a SrO monolayer in contact with the Zintl template. As soon as this SrO layer is formed, we shut off Sr and open Ti while at the same time start increasing the oxygen pressure in order to form a partially oxidized TiO_x layer in contact with the first SrO layer. We keep on increasing the oxygen partial pressure and alternately deposit SrO and TiO_2 to form a few unit cells of STO. At the end of this process, we ideally want to be at a partial pressure where the TiO_2 layer is fully oxidized, which is about 4×10^{-7} Torr when in contact with SrO. We have now formed a thin STO seed layer (two to ten unit cells is commonly used, see Chap. 6) on Si. However, because we used a very low growth temperature, the crystalline quality of this STO seed layer is quite poor and can even be amorphous if the stoichiometry is not perfectly matched. We cannot use a high growth temperature in the presence of oxygen as this can still result in Si oxidation. To improve the crystalline quality, we now remove all oxygen gas in the growth chamber and slowly heat up the STO seed layer to fully crystallize it. Full crystallization typically occurs at around 500 °C

after a few minutes for stoichiometric samples. What we have done then to get around the issue of reactivity of the silicon with oxygen is to kinetically inhibit that process by lowering the substrate temperature when oxygen is present and utilizing the thermodynamic stability of the STO on the template layer to be able to fully crystallize the STO at higher temperature in the absence of oxygen. Normally, to grow crystalline oxides, one needs both a high temperature and high oxygen pressure. But because those conditions also lead to oxidation of the silicon, what we have done is to separate these two conditions in time. We first grow amorphous/poorly crystallized STO with the right stoichiometry at low substrate temperature and sufficiently high oxygen pressure, preventing the formation of SiO_2. Then, we remove oxygen and increase the temperature to provide enough energy so the Sr, Ti, and O atoms find their proper places and form highly crystalline STO, with the oxygen in the STO film staying in STO. Once the crystalline STO seed layer has been formed this way, more STO or even other oxides can be deposited on top of it. Even under conditions of simultaneous high temperature and high oxygen pressure (up to a certain extent), the underlying STO seed layer is perfectly stable and will not be disrupted. Using the optimized conditions for layer-by-layer growth of STO on the STO seed layer grown on Si, some interfacial SiO_2 formation (~1–2 nm) does occur subsequently depending on the seed layer thickness, but this does not at all affect the initial STO seed layer quality. One last thing to note is that the seed layer is naturally oxygen deficient by virtue of the less than optimal initial oxygen pressure used to form it. This is usually healed by subsequent oxide deposition on the seed layer.

2.4 Twinning and Other Rotten Apples

Even if we resolve the wetting issue there still is a problem with the lattice symmetry mismatch between an oxide and semiconductor, in particular if you would like to grow a semiconductor on an oxide substrate. The difference in lattice symmetry brings up additional difficulties. For example, a zincblende material such as GaAs or a diamond-type material such as Si does not possess fourfold symmetry (i.e. the atomic positions are different when you rotate the cell by 90°) while a cubic perovskite oxide such as STO does. Therefore, even the two-dimensional nucleation of GaAs on STO would result in the formation of so-called twin boundaries. Simply put, the STO surface does not have anything to provide GaAs a directional preference. Thus, it can nucleate in one direction in one area of the terrace, and in an orthogonal direction somewhere else on the same terrace. When two such regions meet there will be a domain boundary. In Fig. 2.7 we show two different regions of GaAs on STO, where one region is rotated 90° with respect to another region.

For majority carrier devices (i.e. a transistor) some density of domains in GaAs can be tolerated. However, for minority carrier devices (especially light emitting diodes (LEDs) and lasers), domains are highly undesirable as they lead to reduction

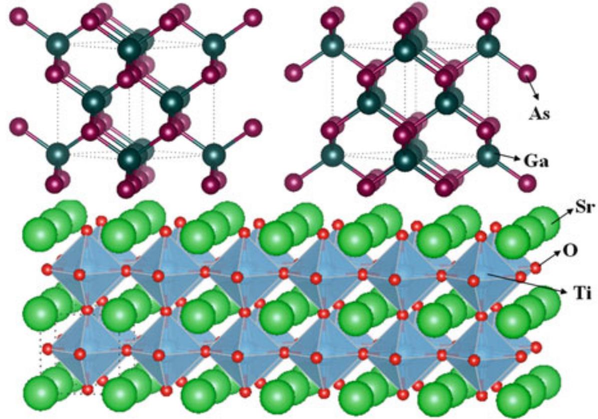

Fig. 2.7 Schematic of nucleation of two orthogonal domains of GaAs on STO

of minority carrier lifetime and non-radiative recombination processes. In order to avoid the formation of twin domains, one needs to provide a preferred direction on the oxide surface; in other words, break the fourfold symmetry of the cubic phase. One possibility is to use vicinal oxide surfaces where step edges may define a preferred nucleation direction. In GaAs epitaxy in Si, double steps are used to eliminate anti-phase domains. These are different type defects; the presence of a single step on a Si surface causes a Ga plane to meet an As plane along the step edge. Orthogonal domains we discuss here are of twin nature; the so-called diamond zig-zag chains meet at a 90° angle on the same terrace of the oxide surface. Though beneficial in that respect and also in reducing the threading dislocation density, the steps on a vicinal surface present a special challenge for oxide/semiconductor epitaxy as we will discuss in the next section. It will also be interesting to explore the role of step edges in selective chemisorption and whether strain can be used to drive a directional nucleation on the oxide surface.

Epitaxy is still possible in some cases even if the crystal symmetries are not totally compatible, for example, growing an orthorhombic material on either a cubic substrate or hexagonal substrate. In such cases, however, the material with lower symmetry grown on a substrate with higher symmetry will form orientation domains. These domains may or may not be detrimental depending on the specific application. One example is the growth of Gd_2O_3 on Si(100). Gd_2O_3 has a bixbyite structure (see Sect. 2.1) with a lattice constant of 10.82 Å, which is 0.4 % smaller than twice the Si lattice constant of 5.43 Å. However, because of interface energy considerations, Gd_2O_3 grows with the 110 orientation on Si(100). The 110 surface unit cell of bixbyite is rectangular-shaped and has twofold symmetry, with the long side having a lattice constant of 15.30 Å and the perpendicular side having a lattice constant of 10.82 Å. The longer side fits almost perfectly with four multiples of the Si(100) surface unit cell length of 3.84 Å (i.e. $4 \times 3.84 = 15.36 \sim 15.30$). However, this nice atomic matching of Si and O along one direction comes at a price of an incommensurate match between the shorter side of the bixbyite surface unit cell and the Si(100) surface unit cell. The epitaxial relationship is Gd_2O_3[110]//Si[110]

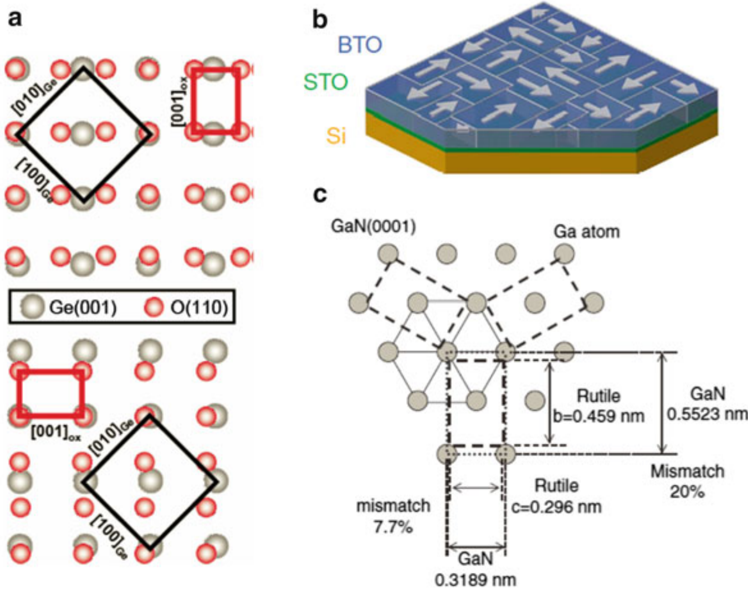

Fig. 2.8 (**a**) Two possible domains of (110) bixbyite on (100) Si/Ge. Copyright IOP Publishing. Reproduced from [47] by permission of IOP Publishing. All rights reserved; (**b**) domains in *a*-axis oriented BTO grown on Si. Reprinted by permission from Macmillan Publishers Ltd: [48], Copyright 2013; (**c**) three possible domains of (100) rutile TiO_2 on (0001) GaN. Reprinted from [49]. Copyright 2005, The Japan Society of Applied Physics

and Gd_2O_3[100]//Si[−110]. Lattice matching along one direction has been lost in order to reduce the interface energy. Because lattice matching of the long side of the rectangular bixbyite cell can occur in either of the two Si directions (it has square symmetry), there are then two possible domains as shown in Fig. 2.8a [47]. A similar but much more subtle domain structure occurs when growing *a*-axis oriented BTO on Si. Due to a combination of thermal expansion mismatch and strain relaxation, thick BTO films (>20 nm) on Si tend to crystallize such that their polar axis (the *c*-axis) lies in the plane of the film. One of the two *a*-axes also lies in plane and tries to match the Si surface unit cell. As with Gd_2O_3, since the Si has a surface with square symmetry, matching of the *a*-axis of BTO can freely occur in one of two perpendicular directions. This causes the *c*-axis of BTO to point randomly in-plane between the two orthogonal directions resulting in a ferroelectric domain structure like that shown in Fig. 2.8b [48]. A more pronounced example of orientation domains is when TiO_2 with tetragonal rutile structure is grown on wurtzite structure GaN. Rutile is observed to grow in the 100 direction, which has twofold symmetry, on the GaN(0001) surface, which has sixfold symmetry. The epitaxial relationship is TiO_2[010]//GaN[10-10] and TiO_2[001]//GaN[11-20]. There are three possible orientations by which the 100 surface unit cell of rutile can match the atoms on the GaN(0001) surface and this results in three orientation domains as shown in Fig. 2.8c [49].

2.5 Step Edges

Typically, in semiconductor heteroepitaxy such as GaAs/AlAs or Si/SiGe the lattice mismatch in the vertical direction (normal to the interface) is exactly the same as in the lateral direction and is small. Therefore, surface steps present a major difficulty mainly if you grow a zincblende crystal like GaAs, on a diamond lattice such as that of Si. In this case you expect anti-phase domains (APD) running along the step edge [50]. A number of techniques have been proposed to battle this problem, including growth on highly vicinal surfaces with double height steps, to promote self-annihilation of APDs that results in APD-free GaAs on Si [51]. Unfortunately, step edges also cause problems in the case of oxide/semiconductor epitaxy, where matching two materials in the plane, does not in general, provide a corresponding match in the out-of-plane directions.

Consider, for example, the (100) surface of silicon. There are always step edges and terraces present on the surface, even for wafers cut as close as possible to the (100) orientation (nominally flat wafers). One can also cut and polish Si wafers with a particular miscut angle in a specific direction. In this case the surface looks like a staircase. As the miscut angle increases, the terrace width becomes smaller. And highly vicinal surfaces (large miscut angle, for example of 6°) are unstable towards step bunching. Step bunching results in wider terraces separated by higher steps or, in some cases, facets. As will be discussed later in the book, reconstruction of this surface results in formation of silicon dimers. Dimers are arranged in rows running along the (110) direction and separated from each other by so called troughs. The symmetry of the dimerized Si(001) 2×1 surface allows for two distinct types of surface step edges, distinguished by whether the dimerization direction on an upper terrace near a step is normal (Type A) or parallel (Type B) to the step edge [52]. For low miscut angles, the surface is characterized by single-height steps (S_A, S_B) alternating regions of 2×1 and 1×2 periodicity. The S_A single step is shown in Fig. 2.9a. The height of the steps is a quarter of the unit cell of silicon (5.43 Å), or 1.358 Å. This surface cannot have two S_A steps without an intervening S_B step [52–56]. However, at increasing miscut angles, double steps become energetically favored to keep terraces long [52–54]. In the lowest energy configuration (D_B) shown in Fig. 2.9b, dimer rows on all terraces run perpendicular to a step edge [52–56]. These single-domain miscut or *vicinal* Si (001) surfaces are used in semiconductor heteroepitaxy for control of antiphase domain growth and strain relief [57].

A miscut angle of 4° towards [110] is sufficient to produce a surface with only D_B steps [54, 55]. Comparing the reconstruction for nominally flat Si with that of the miscut wafer, one sees the nominally flat wafer is double-domain (2×1 and 1×2), while the 4°miscut wafer exhibits a single-domain reconstruction consistent with dimer rows running perpendicular to the step edge [54, 56]. Analysis of the splitting of the reflection high energy electron diffraction (RHEED) streaks allows for an estimate of terrace length [53–56]. A 4° miscut would produce terraces with a length of 3.86 nm and a step height of 2.71 Å.

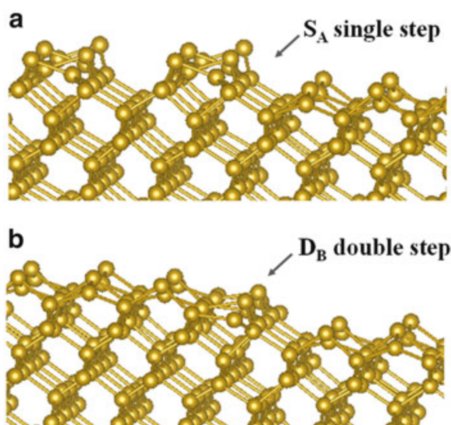

Fig. 2.9 Single and double step on Si (001) surface

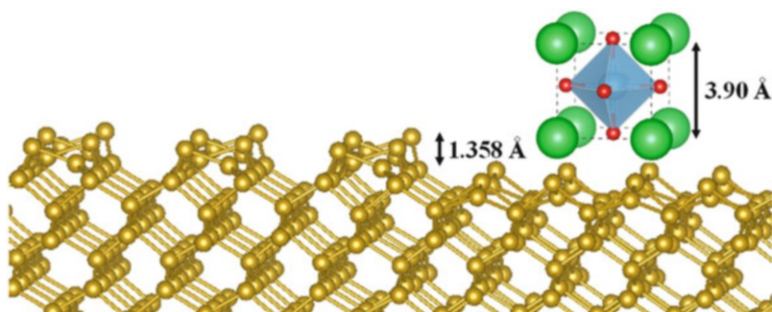

Fig. 2.10 Steps on the silicon (001) surface, a unit cell of ABO_3 perovskite oxide is shown to indicate the height difference

In Fig. 2.10 we show a single S_A step on a Si (001) surface; also shown in the figure is a single unit cell of STO. Laterally the two are well matched (see Fig. 2.2). However, the STO unit cell is 3.9 Å tall, which does not match the step height on the silicon surface! Thus, even under the most ideal situation, STO grown on one silicon terrace may not match the STO grown on an adjacent terrace. This could lead to different domains of STO on the silicon surface with a density of domain walls of 10^{12} cm^{-2} (assuming a typical terrace width of 1,000 Å). As STO is highly ionic, such domain walls are most likely charged and may have adverse effects on materials properties.

The fundamental understanding of what happens as the oxide layers nucleated on different terraces meet at the edge is still largely missing. It is not clear whether the oxide layers grow continuously over step edges, form a line defect along the step edge, or a grain boundary forms along the step edge. Unfortunately, at present, there is still considerable debate about many widely observed grain boundary properties even in bulk perovskites.

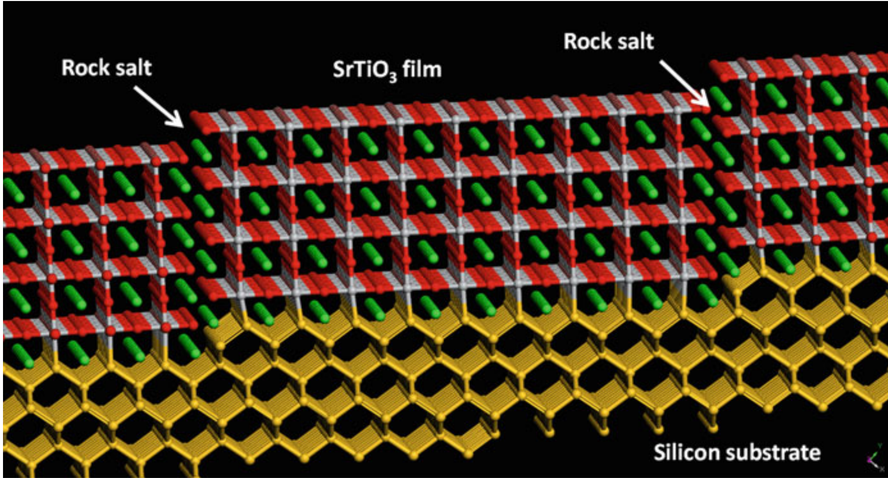

Fig. 2.11 Domain walls at step edges can be healed using the formation of quasi Ruddlesden-Popper layers

High-resolution transmission electron microscope studies and microanalysis results have suggested amorphous phases or cation interstitials to be the origin of the charge imbalance in the boundary plane [58]. More recently, Browning and Pennycook used the combination of Z-contrast imaging and electron-energy-loss spectroscopy (EELS) in the scanning transmission electron microscope (STEM) to study the correlation between the structural and the local electronic properties of STO grain boundaries [59]. They found that (001) tilt grain boundaries contain characteristic sequences of structural units that do not contain any intergranular grain boundary phases [60]. DFT calculations of these units now suggest that the behavior is more complicated than previously thought. In particular, Kim and co-workers found that it is energetically favorable for there to be an excess of oxygen vacancies in these units, and in the case of units centered on the Ti sublattice, a Ti excess [61]. Such non-stoichiometry leads to the formation of a highly doped *n*-type region at the boundary. Recently, Klie et al. have provided direct experimental evidence for the presence of the proposed excess of oxygen vacancies in the grain boundary plane that is independent of the cation arrangement [62].

Growth on a vicinal surface has been performed by Liang and co-workers, who sought to eliminate two-domain formation [63]. They used vicinal substrates with a nominal cutoff angle of 1.2° towards the (110) direction. However, the growth has proven challenging due to high surface reactivity caused by the high step density. A special case may be growth of STO on a 4° miscut Si wafer. Such a miscut towards the <110> direction, results in 3.86 nm wide terraces. That distance is close to approximately ten unit cells of STO. One possible way to heal the domain walls in this case could be the formation of quasi Ruddlesden-Popper planes along the step edge as shown in Fig. 2.11. The Ruddlesden–Popper (RP) type phases of general formula $A_{n+1}B_nO_{3n+1}$ or $AO(ABO_3)_n$ (where A is rare earth/alkaline

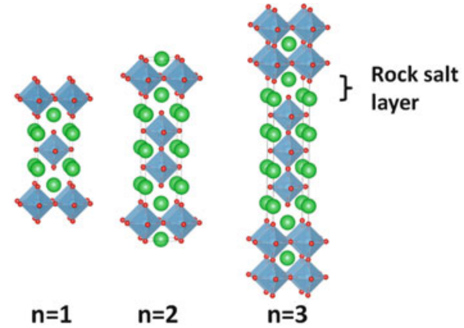

Fig. 2.12 The first three members of the Ruddlesden-Popper series of phases with formula $A_{n+1}B_nO_{3n+1}$

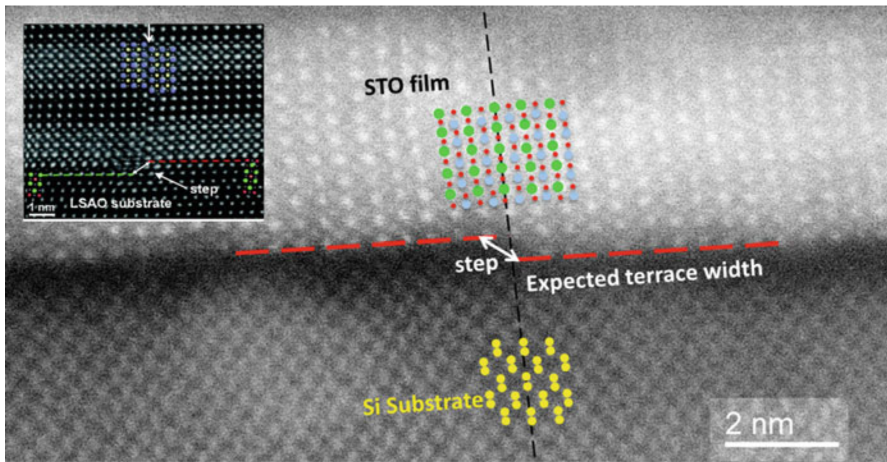

Fig. 2.13 Scanning transmission electron micrograph of STO grown on 4º miscut vicinal Si(100). (Image courtesy of D. J. Smith). *Inset*: a RP fault in $LaNiO_3$ grown across a step of the (La, Sr) AlO_4 substrate. Reprinted with permission from [67]. Copyright 2012, AIP Publishing LLC

earth ion, B is a transition metal ion) [64], crystallize with tetragonal or orthorhombic unit cell in the space group *I4/mmm* or *Fmmm*. The crystal structure of these phases can be described by the stacking of finite n layers of perovskites ABO_3 between rock salt AO layers along the crystallographic c direction. In Fig. 2.12 we show the first three members of this family. The stoichiometric ABO_3 can be viewed as a RP phase with $n = \infty$. RP phases for $SrTiO_3$ can be grown by MBE through precise control of the deposition process [65]. The inclusion of the rocksalt structure at the step edge allows for almost perfect matching of the STO on a Si terrace. The challenge is to stabilize the terrace size during the STO deposition. In Fig. 2.13 we show a STEM image of STO grown on a 4° miscut Si wafer [66]. A RP fault in a $LaNiO_3$ film grown across a step of an LSAT substrate from [67] is shown for comparison. The steps are clearly seen; however, the height appears to be larger than 2.71 Å and the terraces are significantly wider. This is most likely related to step bunching,

often observed in vicinal Si (001) at elevated temperature in the presence of metals [68]. Surprisingly, the STO film appears to grow across the step uninterrupted.

2.6 The Role of the Interface

Assuming we have found a way to achieve monolithic integration of transition metal oxides and semiconductors, a natural question arises: where such hybrid structures may find useful applications. The answer to this question depends on whether it is the integrity of the interface itself or the top oxide layer that is of interest.

One of the benefits of the epitaxial interface is its low defectivity. The most celebrated oxide/semiconductor interface between silicon and silicon dioxide (SiO_2) as grown has only 10^{-10} electrically active defects per cm^2; that number can be reduced to 10^{-12} by a subsequent forming gas anneal that passivates dangling bonds at the interface. However, silicon dioxide is amorphous and dangling bonds at the interface appear at random. Theoretically, an epitaxial interface may be "defect free". One has to be careful with the terminology here, as there is always some equilibrium concentration of point defects controlled by their formation energy and temperature. The term "defect free" therefore implies equilibrium thermodynamic concentration of defects. Therefore an epitaxial oxide could be used instead of SiO_2 as a *gate dielectric*. This indeed was the original motivation of McKee et al. [30] when growing STO on Si. Another example would be using $YMnO_3$ as a ferroelectric gate for GaN [20]. Ironically, none of that came to be.

If one can find a way of growing a semiconductor layer epitaxially on the oxide substrate, and that oxide substrate may be integrated on the same or perhaps, a different semiconductor, one could have the epitaxial analogue of the *silicon on insulator* (SOI) structure. One example of this approach would be integration of Ge on Si using rare earth oxide buffers [18, 19]. An even more intriguing possibility is to use epitaxial oxide layers as buffers in integration of different semiconductors. Thus GaAs has been successfully integrated on Si (001) using an STO buffer [31], and more recently high quality GaN layers have been grown on Si(111) using the bixbyite form of Gd_2O_3 [69].

On the other hand, one can use the oxide layer epitaxially grown on a semiconductor as a *virtual substrate*. STO on Si would be a classic example of this approach. As high quality STO films can be grown on 200 mm Si wafers [70], this effectively opens the door for integrated oxide electronics as STO is a widely used substrate for growing ferroelectric, ferromagnetic and superconducting oxides [71, 72]. Last but not least is the opportunity to create novel oxide or hybrid heterostructures on semiconductor substrates. One such example would be photocatalytic structures integrated on Si (001) [73].

We are now at a point in time where the necessary technology is available to model, fabricate, and measure these functional oxides epitaxially integrated with semiconductors. In the next three chapters will briefly describe this necessary know-how before going into detail on actual epitaxial oxide on semiconductor systems.

References

1. J.Y. Tsao, *Materials Fundamentals of Molecular Beam Epitaxy* (Academic, San Diego, CA, 1993)
2. R.M. Sieg, S.A. Ringel, S.M. Ting, S.B. Samavedam, M. Curie, T. Lando, E.A. Fitzgerald, J. Vac. Sci. Technol. B **16**, 1471 (1998)
3. Y.H. Lo, Appl. Phys. Lett. **59**, 2311 (1991)
4. Z. Yang, J. Alperin, W.I. Wang, S.S. Iyer, T.S. Kuan, F. Semendy, J. Vac. Sci. Technol. B **16**, 1489 (1998)
5. C. Carter-Coman, A.S. Brown, N.M. Jokerst, D.E. Dawson, R. Bicknell-Tassius, Z.C. Feng, K.C. Rajkumar, G. Dagnall, J. Electron. Mater. **25**, 1044 (1996)
6. Z. Yang, F. Guarin, I.W. Tao, W.I. Wang, S.S. Iyer, J. Vac. Sci. Technol. B **13**, 789 (1995)
7. J.W. Matthews, A.E. Blakeslee, J. Cryst. Growth **27**, 118 (1974)
8. R. People, J.C. Bean, Appl. Phys. Lett. **47**, 322 (1985)
9. T.E. Whall, E.H.C. Parker, J. Phys. D **32**, 1187 (1999)
10. S.B. Adler, J. Am. Ceram. Soc. **84**, 2117 (2001)
11. H. Seo, A. Posadas, A.A. Demkov, Phys. Rev. B **86**, 014430 (2012)
12. L. Qiao, T.C. Droubay, T. Varga, M.E. Bowden, V. Shutthanandan, Z. Zhu, T.C. Kaspar, S.A. Chambers, Phys. Rev. B **83**, 085408 (2011)
13. V.V. Mehta, M. Liberati, F.J. Wong, R.V. Chopdekar, E. Arenholz, Y. Suzuki, J. Appl. Phys. **105**, 07E503 (2009)
14. L. Qiao, T.C. Droubay, M.E. Bowden, V. Shutthanandan, T.C. Kaspar, S.A. Chambers, Appl. Phys. Lett. **99**, 061904 (2011)
15. M.L. Yu, B.N. Eldridge, Phys. Rev. Lett. **58**, 1691 (1987)
16. N. Shimizu, Y. Tanishiro, K. Takayanagi, K. Yagi, Surf. Sci. **191**, 28 (1987)
17. J.C. Woicik, H. Li, P. Zschack, E. Karapetrova, P. Ryan, C.R. Ashman, C.S. Hellberg, Phys. Rev. B **73**, 024112 (2006)
18. H.J. Osten, A. Laha, M. Czernohorsky, E. Bugiel, R. Dargis, A. Fissel, Phys. Status Solidi A **205**, 695 (2008)
19. R. Dargis, A. Fissel, D. Schwendt, E. Bugiel, J. Krügener, T. Wietler, A. Laha, H.J. Osten, Vacuum **85**, 523 (2010)
20. A. Posadas, J.-B. Yau, C.H. Ahn, J. Han, S. Gariglio, K. Johnston, K.M. Rabe, J.B. Neaton, Appl. Phys. Lett. **87**, 171915 (2005)
21. H.R. Child, R.M. Moon, L.J. Raubenheimer, W.C. Koehler, J. Appl. Phys. **38**, 1381 (1967)
22. R.M. Moon, W.C. Koehler, Phys. Rev. B **11**, 1609 (1975)
23. M. Badylevich, S. Shamuilia, V.V. Afanas'ev, A. Stesmans, A. Laha, H.J. Osten, A. Fissel, Appl. Phys. Lett. **90**, 252101 (2007)
24. B.J. Kennedy, M. Avdeev, Aust. J. Chem. **64**, 119 (2011)
25. A.A. Stekolnikov, J. Furthmüller, F. Bechstedt, Phys. Rev. B **65**, 115318 (2002)
26. J. Padilla, D. Vanderbilt, Surf. Sci. **418**, 64 (1998)
27. X. Zhang, A.A. Demkov, H. Li, X. Hu, Y. Wei, J. Kulik, Phys. Rev. B **68**, 125323 (2003)
28. K. Johnston, M.R. Castell, A.T. Paxton, M.W. Finnis, Phys. Rev. B **70**, 085415 (2004)
29. M.R. Castell, Surf. Sci. **505**, 1 (2002)
30. R.A. McKee, F.J. Walker, M.F. Chisholm, Phys. Rev. Lett. **81**, 3014 (1998)
31. K. Eisenbeiser, R. Emrick, R. Droopad, Z. Yu, J. Finder, S. Rockwell, J. Holmes, C. Overgaard, W. Ooms, IEEE Electron. Device Lett. **23**, 300 (2002)
32. A.A. Demkov, X. Zhang, J. Appl. Phys. **103**, 103710 (2008)
33. E. Zintl, W. Dullenkopf, Z. Phys. Chem. B **16**, 195 (1932)
34. A.A. Demkov, H. Seo, X. Zhang, J. Ramdani, Appl. Phys. Lett. **100**, 071602 (2012)
35. K. Seino, W.G. Schmidt, F. Bechstedt, J. Bernholc, Surf. Sci. **507–510**, 406 (2002)
36. Y. Liang, J. Kulik, T.C. Eschrich, R. Droopad, Z. Yu, P. Maniar, Appl. Phys. Lett. **85**, 1217 (2004)
37. Y. Liang, J. Curles, M. McCready, Appl. Phys. Lett. **86**, 082905 (2005)

38. A. Slepko, A.A. Demkov, Phys. Rev. B **85**, 195462 (2012)
39. L. Schlipf, A. Slepko, A.B. Posadas, H. Seinige, A. Dhamdhere, M. Tsoi, D.J. Smith, A.A. Demkov, Phys. Rev. B **88**, 045314 (2013)
40. F.J. Walker, R.A. McKee, J. Cryst. Growth **116**, 235 (1992)
41. J. Lettieri, J.H. Haeni, D.G. Schlom, J. Vac. Sci. Technol. A **20**, 1332 (2002)
42. M.H. Yang, C.P. Flynn, Phys. Rev. Lett. **62**, 2476 (1989)
43. C.M. Brooks, L. Fitting Kourkoutis, T. Heeg, J. Schubert, D.A. Muller, D.G. Schlom, Appl. Phys. Lett. **94**, 162905 (2009)
44. N.A. Braaten, J.K. Grepstad, S. Raaen, S.L. Qui, Surf. Sci. **250**, 51 (1991)
45. E.G. Keim, L. Wolterbeek, A. Van Silfhout, Surf. Sci. **180**, 565 (1987)
46. Y. Liang, S. Gan, M. Engelhard, Appl. Phys. Lett. **79**, 3591 (2001)
47. A. Molle, C. Wiemer, M.D.N.K. Bhuiyan, G. Tallarida, M. Fanciulli, J. Phys. **100**, 042048 (2008)
48. S. Abel, T. Stöferle, C. Marchiori, C. Rossel, M.D. Rossell, R. Erni, D. Caimi, M. Sousa, A. Chelnokov, B.J. Offrein, J. Fompeyrine, Nat. Commun. **4**, 1671 (2013)
49. T. Hitosugi, Y. Hirose, J. Kasai, Y. Furubayashi, M. Ohtani, K. Nakajima, T. Chikyow, T. Shimada, T. Hasegawa, Jpn. J. Appl. Phys. **44**, L1503 (2005)
50. J.B. Posthill, J.C.L. Tarn, K. Das, T.P. Humphreys, N.R. Parikh, Appl. Phys. Lett. **53**, 1207 (1988)
51. K. Adomi, S. Strite, H. Morkoç, Appl. Phys. Lett. **56**, 469 (1990)
52. D. Chadi, Phys. Rev. Lett. **59**, 1691 (1987)
53. K. Sakamoto, T. Sakamoto, J. Electrochem. Soc. **136**, 2705 (1989)
54. E. Pehlke, J. Tersoff, Phys. Rev. Lett. **67**, 465 (1991)
55. D. Saloner, J.A. Martin, M.C. Tringides, D.E. Savage, C.E. Aumann, M.G. Lagally, J. Appl. Phys. **61**, 2884 (1987)
56. J. Reiner, K. Garrity, F.J. Walker, S. Ismail-Beigi, C.H. Ahn, Phys. Rev. Lett. **101**, 1 (2008)
57. F. Riesz, J. Vac. Sci. Technol. A **14**, 425 (1996)
58. Y.M. Chiang, T. Takagi, J. Am. Ceram. Soc. **73**, 3278 (1990)
59. N.D. Browning, S.J. Pennycook, J. Phys. D **29**, 1779 (1996)
60. M.M. McGibbon, N.D. Browning, M.F. Chrisholm, A.J. McGibbon, S.J. Pennycook, V. Ravikumar, V.P. Dravid, Science **266**, 102 (1994)
61. M. Kim, G. Duscher, N.D. Browning, K. Sohlberg, S.T. Pantelides, S.J. Pennycook, Phys. Rev. Lett. **86**, 4056 (2000)
62. R.F. Klie, M. Beleggia, Y. Zhu, J.P. Buban, N.D. Browning, Phys. Rev. B **68**, 214101 (2003)
63. Y. Liang, Y. Wei, X.M. Hu, Z. Yu, R. Droopad, H. Li, K. Moore, J. Appl. Phys. **96**, 3413 (2004)
64. S.N. Ruddlesden, P. Popper, Acta Crystallogr. **11**, 54 (1958)
65. J.H. Haeni, C.D. Theis, D.G. Schlom, W. Tian, X.Q. Pan, H. Chang, I. Takeuchi, X.-D. Xiang, Appl. Phys. Lett. **78**, 3292 (2001)
66. K. Kormondy, private communication
67. E. Detemple, Q.M. Ramasse, W. Sigle, G. Cristiani, H.-U. Habermeier, B. Keimer, P.A. van Aken, J. Appl. Phys. **112**, 013509 (2012)
68. H.-C. Jeong, E.D. Williams, Surf. Sci. Rep. **34**, 171 (1999)
69. F.E. Arkun, M. Lebby, R. Dargis, R. Roucka, R.S. Smith, A. Clark, ECS Trans. **50**, 1065 (2013)
70. X. Gu, D. Lubyshev, J. Batzel, J.M. Fastenau, W.K. Liu, R. Pelzel, J.F. Magana, Q. Ma, V.R. Rao, J. Vac. Sci. Technol. B **28**, C3A12 (2010)
71. C. Dubourdieu, J. Bruley, T.M. Arruda, A. Posadas, J. Jordan-Sweet, M.M. Frank, E. Cartier, D.J. Frank, S.V. Kalinin, A.A. Demkov, V. Narayanan, Nat. Nanotechnol. **8**, 748 (2013)
72. A.B. Posadas, C. Mitra, C. Lin, A. Dhamdhere, D.J. Smith, M. Tsoi, A.A. Demkov, Phys. Rev. B **87**, 144422 (2013)
73. T.Q. Ngo, A. Posadas, H. Seo, S. Hoang, M.D. McDaniel, D. Utess, D.H. Triyoso, C. Buddie Mullins, A.A. Demkov, J.G. Ekerdt, J. Appl. Phys. **114**, 084901 (2013)

http://www.springer.com/978-1-4614-9319-8

Integration of Functional Oxides with Semiconductors
Demkov, A.A.; Posadas, A.B.
2014, X, 278 p. 146 illus., 113 illus. in color., Hardcover
ISBN: 978-1-4614-9319-8